IC 225

K. WEBB

Department of Physics and Astronomy, University of Victoria, Victoria, B.C. V9B5M3, Canada
Draft version September 11, 2015

ABSTRACT

Your abstract.

1. INTRODUCTION

Dwarf elliptical (dE) galaxies are the most numerous population in high density environments (Ferguson and Binggeli 1994) yet until recently they have been poorly studied due to the observational challenges posed by their and low surface brightness. Only with recent large scale surveys has there been insight into the formation and evolution processes of these early type galaxies (ETGs). Bright, high mass ETGs are known to follow well defined scaling relations linking structure, kinematics, and stellar population histories. There is much interest in assessing whether dEs experience similar processes, and if they 'bridge the gap' between the faintest and most massive galaxies. Observations with 2D spectroscopy suggests that the inner structure of dEs is surprisingly complex (e.g. spiral arms, kinematically decoupled cores (KDCs), multiple gaseous components) with a variety of kinematic properties and stellar population ages and metallicities (SAURON Sarzi et al. 2006, ATLAS^{3D} Cappellari et al. 2011, CALIFA Sánchez et al. 2012, NGVCS Guérou et al. 2015). Through a study of the internal dynamics and stellar population histories it is possible to discern the formation and evolution processes of dEs. Determining whether or not they are progenitors of the most massive galaxies, as predicted by the lambda cold dark matter (ΛCDM) hierarchical merging model would have important consequences for the constraints on the galaxy luminosity function and cosmological models (Ferguson and Binggeli 1994, and references therein).

Many bright dEs contain a star cluster-like nuclei – where the formation of these nuclei are also poorly understood. Unlike massive ellipticals, dE nuclei are typically bluer than the rest of the galaxy, and have colours similar to the stellar populations in nearby globular clusters (Lotz et al. 2004). It has been suggested that the nuclei formed from gravitationally bound globular clusters falling into the potential well of the dE, or that infalling gas collected and sustained continued star formation. However, some dEs have been observed to have signif-

icantly bluer nuclei than expects, suggesting much more recent star formation - such as caused by nuclear starbusts, dynamical friction via mergers of globular clusters, or tidal stripping or harassment of spiral galaxies lotz01. Each scenario makes certain predictions for the kinematic structure and stellar populations, and with two-dimensional spectroscopic imaging we can distinguish between the various formation models.

Central velocity dispersions consistent with early measurements (Bender and Nieto 1990; Peterson and Caldwell 1993; Geha et al. 2002) would suggest a mass-luminosity relation consistent with supernova driven wind models required for strong feedback in the ΛCDM model. Strong rotation is increasingly being observed for many flattened dEs (van Zee et al. 2004; Rojas et al. 2004; de Rijcke et al. 2005), where rotational flattening would be expected from harassment events in which the system was heated, increasing the velocity dispersion. Complex substructure such as spiral features and kinematically decoupled cores (KDCs, where the core has a separate rotation axis than that of the galaxy), in addition to high rotation, could indicate that bright dEs evolved from stripped or harassed spirals. A complement to the kinematic structure in distinguishing formation scenarios is the 2D stellar population information. For example, a KDC of similar age but lower metallicity would be the result of a dissapationless merger whereas a young stellar population would be expected from a starburst as a result of a dissipative merger. Alternatively, a spin up interaction would show no population change.

In this paper we present a study of the bright ($M_B = -17.14$) dE galaxy IC 225 to determine the processes within the center of the galaxy. With two-dimensional spectroscopic data we can determine the source and extent of the ionized gas, as well as the kinematics in relation to the underlying stellar population, and analyze the ages and metallicities of the stellar populations.

IC 225 is relatively nearby (20.6 Mpc), with redshift 1535 km/s, and isolated – no observable companion

within 30' was found in the NASA/IPAC Extragalactic Database (NED) (Gu et al. 2006). It is peculiar in that it has a double nucleus separated by 1.4" and a very blue core indicating ongoing star formation despite being largely devoid of HI gas (Gu et al. 2006, and references therein). Strong nebular emission lines have been noted in the central 4-5" (Augarde et al. 1994; Gu et al. 2006) with a 0.5Å($\sim$25 $^{km}/_s$) blue shift in the emission lines. Gu et al. (2006) proposes that the emission lines are associated with the possibly kinematically decoupled offset nucleus while the absorption is associated with the central source. IC 225 is also found to have a high oxygen abundance in the central photoionized gas of $12 + log(O/H) = 8.9$, $\sim 0.78\,dex$ greater than expected from the luminosity-metallicity relations for dwarfs (Gu et al. 2006).

In this paper we use two-dimensional spectroscopic data of IC 225 to compare various reduction procedures for the Gemini Multi Object Spectrograph (GMOS, Hook et al. 2004) Integral Field Unit (IFU, Allington-Smith et al. 2002), as well as analyze the differences between several kinematic measurement techniques, and explore the functionality of a full-spectrum fitting procedure for stellar population analysis. This is a continuation of a project by G. Rudie and B. Miller (Rudie 2006) where we reproduce their results with improved reduction techniques, and provide additional analysis of the kinematics and stellar population history.

2. DATA

2.1. *Observations*

Observations of IC 225 were obtained from the 8.1 m Gemini North Observatory with the GMOS IFU in two slit mode between December 5th and 23rd 2005 under the program GN-2005B-DD-5. The GMOS-IFU in two slit mode provides a 7"x5" field of view (FOV) and with 1000 hexagonal lenslets for the science target, with an additional 500 lenslets with a 5"x3.5" FOV approximately 1 arcmin away from the science field for a measure of the sky background level. Each lenslet passes light through two slits, with both slits cover half the total FOV, and the light is then dispersed with the grating of choice for the desired spectral coverage.

Figure 1. Sloan Digital Sky Survey colour image of IC 225 with scale 2"x2" which shows the red hue of the galaxy and the blue central core.

Four exposures where taken, each for 3300 seconds, using the B600 grating and g-filter. This grating and filter combination has two central wavelengths, 482 nm and 478 nm, which provides a wavelength coverage of 4200-5400Åwhere strong stellar absorption lines such as the Balmer lines (Hβ, and Hγ) and the [OIII]$\lambda\lambda$4959,5007 doublet are observed. The data were reduced as described in the following section.

2.2. *Data Reduction*

This data set was used to compare several reduction techniques, where the results from the best reduction procedure were used for the following analysis. We consider four different techniques: a method used with the same observations of IC 225 with a modified version of the Gemini[1] IRAF[2] package v1.9 and a previously standard reduction procedure performed by Rudie (2006); with the recently released Gemini IRAF package v1.12 available with the Ureka[3] v1.5.1 installation and an updated reduction procedure with and without twilight flats; and using the same procedure but with several modified Gemini GMOS IRAF tasks we refer to as *ifudrgmos* still under development but available in partial in the recent release of the Gemini IRAF package v1.13. In all cases the reduction includes: bias and overscann subtraction; masking and correcting bad pixels; flat-field extraction; scattered light subtraction; cosmic-ray cleaning; wavelength calibration; and sky subtraction. The order in which the steps are applied differ between the old and the current reduction procedures to incorporate new functions available in the latest Gemini package.

The parameter chosen to evaluate each procedure was the minimization of a slight velocity dispersion between the two slits of the IFU. This is thought to result from a slight irregularity in the illumination of the slits due to the optics of the instrument, and is shown in figure 2. The shift is calculated from a simple statistical difference between the two slits in the arc spectrum, and the difference is corrected for in the science images.
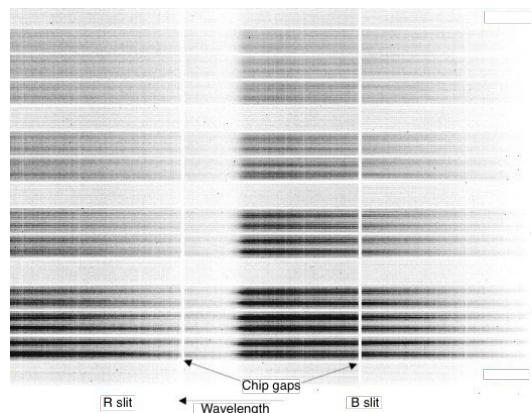
Figure 2. A diagram of the IFU object field showing the three CCD mosaic with the chip gaps. The illumination difference between the slits is made obvious here, where the right slit has higher average throughput than the left slit.

The observation of IC 225 we use in our analysis were first processed by Rudie (2006) with an unofficial modified version of the previous Gemini IRAF package v1.9.

---

[1] https://www.gemini.edu
[2] http://iraf.net
[3] http://ssb.stsci.edu/ureka

The preliminary reduction steps were processed with an early version of the unofficial task `ifuproc` developed by B. Miller (personal communication).

To determine the difference between the previous version of the Gemini IRAF tasks and the current package, we repeat the reduction with a similar procedure. We use an updated version of `ifuproc` which takes into account the new capabilities of the Gemini tasks and eliminates some of the parameters in the modified v1.9 not included in the update to v1.12. We perform this reduction both with and without twilight flats to explore the effects of possible dark and bright bands due to difference in the fiber flexure between the science and twilight observations, and determine if including the twilight correction provides a significant improvement in the reduction. This is important as our last reduction procedure (see below) is not currently capable of handling twilight images. We expect that the GCal flatness over the IFU field will not vary by more than a few percent and the twilight correction will be negligible.

Our last procedure involves the same reduction steps as the previous technique, except that we use a revised version (56) of the Gemini IRAF package provided by James Turner and Bryan Miller via the Gemini Data Reduction User Forum[4]. The majority of the revised tasks in this package are available in the recently released v1.13 package, though most notably lacking the improved fibre throughput correction algorithm. At this time the task is unable to process twilight exposures, so instead we process our twilight frames as science images and manually inspect for pixel-to-pixel variations across what we expect to be a homogeneously illuminated field, and determine the small variation in the field to be satisfactory. Additional details regarding this procedure can be found in Davies et al. (2015).
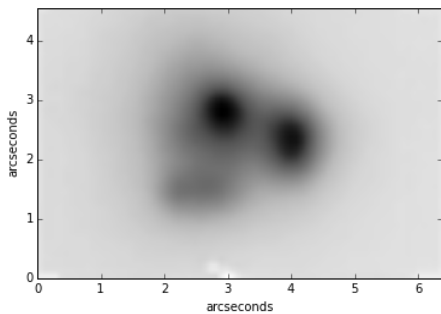
Figure 3. GMOS IFU image of IC 225 collapsed across the entire observed wavelength range. Three central flux sources are observed: a central nucleus, an off-center nucleus to the right, and a tertiary dim flux source.

2.3. *Wavelength shift minimization*

The calculated shift as calculated for each reduction method is presented in Table 1. We find that the best reduction method is the updated reduction procedure with the *ifudrgmos* as it best minimizes the velocity shift of the two slits in addition to including an improved flat field correction procedure. The specific details of this reduction procedure, with the modifications of `ifudrgmos`

[4] http://drforum.gemini.edu

to the publicly available Gemini IRAF package, are described in the Appendix.

2.4. *Merging*

The exposures were transformed from 2D maps of wavelength and fibre number to a 3D cube of spatial and spectral dimensions across the galaxy. Each cube was examined for significant noise features at the bounds of the observed spectrum, and cropped to a common wavelength range. The cubes were then spatially aligned with the PyFu 3D data manipulation package v0.8.1, developed by James Turner though the Gemini Data Reduction User Forum, which determines the relative pixel shift of each exposure by mutual pointings and/or spectral offsets. Despite the slight ($\leq 3^{km/s}$) difference in relative heliocentric velocity between our first and last exposures, we expect this to be insignificant to our analysis with respect to our measurement uncertainties and do not apply a correction before combining the four exposures into the final data cube with the PyFu package. A collapsed wavelength image of our final cube is shown in figure 3, where we observe three central flux sources.

2.5. *Reduction issues specific to our observations*

For our observations of IC 225 we had the case that, for the majority of our IFU spectra, the OIII emission line fell almost directly on the right hand chip gap shown in figure 2. This caused an issue in the interpolation of the continuum when the three CCDs were mosaiced together in the reduction procedure. This issue was common to all the reduction methods, yet was minimized in our chosen reduction method with `fudrgmos`.

This additional noise feature introduces an issue when fitting a simple stellar population (SSP) to our galaxy spectra, as well as presents additional difficulty when we later manually remove the emission lines to obtain a pure-absorption spectra. As a result, we take additional considerations when preforming the analysis for this set of observations.
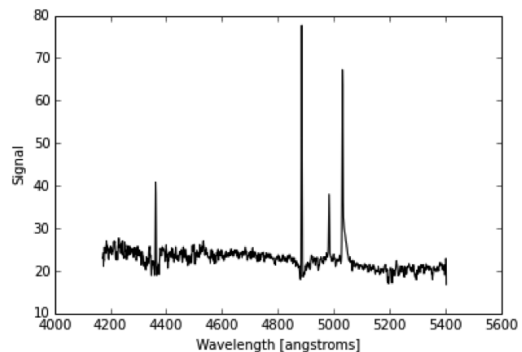
Figure 4. An example spectrum illustrating the interpolation error over the chip gap. This resulting in an additional feature on or next to the OIII emission line at 5042λ.

3. ANALYSIS

3.1. *Ionized gas distribution*

In order to observe the relative flux of our image plane in several spectral regions of interest, the cube was collapsed to 2D spatial maps for select wavelength ranges

Reduction method	Avg. arc vel. diff. $[km/s]$
Previous procedure and GMOS pkg. v1.9	6.5038 ± 3.3523
Revised procedure and GMOS pkg. v1.12 w. twilights	6.3258 ± 3.2507
Revised procedure and GMOS pkg. v1.12 w/o. twilights	6.3254 ± 3.2578
Revised procedure and *ifudrgmos* pkg.	6.2290 ± 3.1825

Table 1
Velocity shift measurements between the two slits measured for two arcs for each reduction procedure. We determine the best procedure from that which minimizes this shift.

as shown in figure 5. This process is roughly equivalent to observing the galaxy in several different filters. Three sources are distinct in the continuum range (see figure 5(a)): a central nucleus, a off-center nucleus, and a tertiary dim flux source - where the central nucleus is the most luminous. The strongest features observed in the spectra of IC 225 are the nebular emission lines Hβ, Hγ, and the [OIII] doublet. In each of the emission maps (figure 5(b,c,d) the off-center nucleus is much more luminous than the central nucleus, indicating that this region has a significant emitting gaseous region associated with it.

3.2. *Binning*

To increase the signal-to-noise (S/N) of our data above a minimum level required for robust measurements of the kinematics and stellar population histories we applied a spectral binning routine. For the analysis with the emission features, we used an adaptive spatial binning software[5] (Cappellari and Copin 2003). The spectra are co-added in order of closest to the bin centroid, and the application of Voronoi tessellation (Du et al. 1999) such that the S/N of the faint regions is relatively uniform, and the bins are compact and non-overlapping. We select a S/N minimum of 20 for our analysis as our emission lines are quite strong.The binning scheme for the emission line analysis is shown in figure 6(a).

For the stellar population analysis we were interested in the specific properties of the three bright flux sources observed in the 2D maps (refer to figure 3) it was necessary to ensure that each source was assigned to its own bin. This was achieved by adapting the Voronoi bin map in the region of the sources while preserving the surrounding bins. We can therefore directly compare the kinematics and history information of each source. With the background evenly divided so as to obtain a uniform S/N of ~25 (and arranged in a pattern to best observe rotation) and bins over the central sources of S/N ~40 we measure the stellar kinematics (see figure 6(b)). For stellar population histories we combine the background bins such that we raise the S/N to ~40 (see figure 6(c)).

4. KINEMATICS

Within the limited wavelength range of our IFU observations (4173-5405Å) we detected the strong emission lines of Hγ, Hβ, and the [OIII] doublet. This introduced an issue when measuring the stellar population kinematics as the emission lines were very close to or coincident with the most age- or metallicity-sensitive absorption features. In masking the emission affected regions the absorption features would be excluded, which would not be ideal when there is insufficient information in the emission-free part of the spectrum to adequately constrain the stellar population content - such as for our data. To circumvent this issue we consider three different routines for the measurement of the stellar velocities where the emission lines are instead removed from the galaxy spectra - a direct pixel-fitting (pPXF) technique (Cappellari and Emsellem 2004) and two cross-correlation fitting techniques available in the RV IRAF, and the RVSAO IRAF packages.

For the gas kinematics no such issue of contamination exists. As the emission lines are significantly stronger than the absorption features, we can consider our galaxy spectra as approximately equivalent to a pure emission spectra.
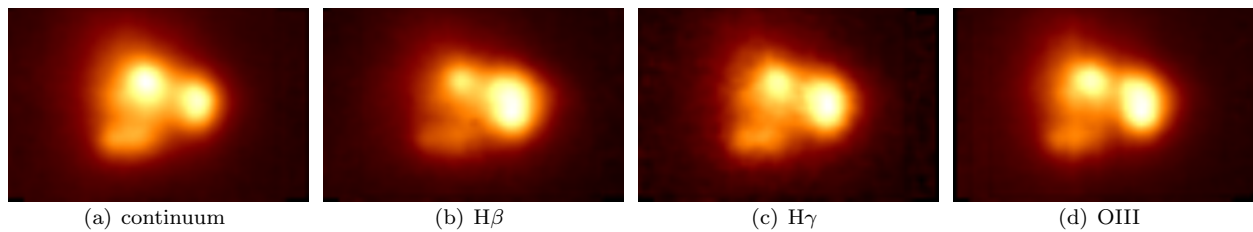
4.1. *Measurement routines*

pPXF[6] is a penalized pixel-fitting routine (Cappellari and Emsellem 2004) which is capable of differentiating the emission and absorption features, and effectively mask the emission regions from the fitting process. In this routine an optimal spectral template is determined from a bounded least-square fitting algorithm which iteratively fits the galaxy spectrum with a linear combination of stellar templates from an empirical library of stars to create an optimal (best-fit) template. A line-of-sight velocity distribution (LOSVD) is them parameterized from the optimal template, and the kinematics (velocity, velocity dispersion, and higher order parameters) are then extracted from the LOSVD. Although robust against the presence of emission lines, this method is sensitive to template mismatch - unlike cross correlation which minimizes the coupling between different absorption features by restricting the analysis to the main peak of the cross-correlation between the template and the galaxy spectra. It is necessary to select a template spectra which closely matches the galaxy spectra for robust and reliable measurements. For our data set we select the MILES library (Vazdekis et al. 2010; Sánchez-Blázquez et al. 2006) which covers a spectral range of 3525-7500 Åat a resolution of 2.5 ÅFWHM ($\sigma = 60\frac{km}{s}at5000$ Å) which is slightly lower than the GMOS-IFU spectral resolution of 2.1 ÅFWHM. We also implement a penalization into out pPXF routine which avoids undersampling by biasing the solution towards a Gaussian automatically as a function of the S/N and the velocity distribution (see Emsellem et al. (2004)).

We estimate the errors with a Monte Carlo method in which a Poisson noise is included for many realizations of the measurement of the kinematics from the galaxy spectrum. Figure **??** summarizes the results from such simulations. For S/N of ~40 the errors on the velocity is

---

[5] http://www-astro.physics.ox.ac.uk/ mxc/software/

[6] http://www-astro.physics.ox.ac.uk/ mxc/software/

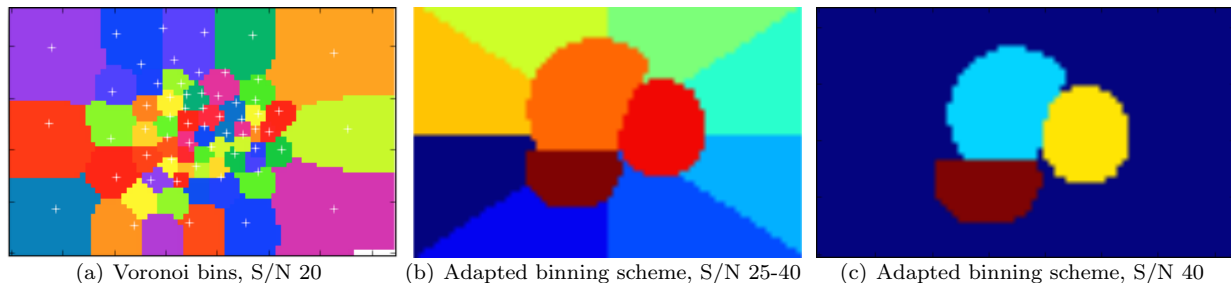(a) continuum   (b) Hβ   (c) Hγ   (d) OIII

Figure 5. Continuum and ionized gas maps of IC 225 of dimensions 5x7 arcsecs. We note that the relative luminosity of the off center nucleus is greater than the of the central nucleus in the maps of the emission regions.

(a) Voronoi bins, S/N 20   (b) Adapted binning scheme, S/N 25-40   (c) Adapted binning scheme, S/N 40

Figure 6. Binning schemes for the kinematic analysis of the gas (a), and stellar population (b), and for the stellar population histories analysis (c). The bin colours were chosen only to best distinguish the boundaries. In figure (a) the white crosses refer to the bin centroids as calculated by the Voronoi binning routine.

$\sim$12 km/s and on the velocity dispersion $\sim$20 km/s.
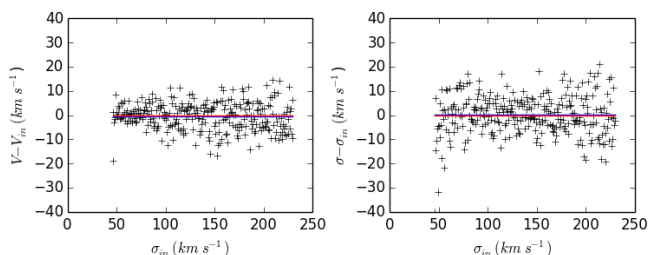
Figure 7. Simulated errors on the measured stellar population velocity (left) and velocity dispersion (right) using Monte Carlo realizations for S/N 40. The red line shows the zero baseline, where the blue line is the mean of the data points.

We also use the IRAF tasks `rv.fxcor`, `rvsao.xcsao` (absorption line fitting) and `rvsao.emsao` (emission line fitting) with as near as equivalent parameters as possible to measure the kinematics by cross-correlation of the pure absorption or pure emission spectra. Although the `rvsao` package tasks include an algorithm to chop the emission features from the spectra, we find its implementation to cause the cross correlation fit to give erroneous measurements of the velocity. Instead we develop a routine to fit an remove the emission lines from our galaxy spectra, which is described in detail in the Appendix. For the cross correlation routines we measured the velocities relative to the central nuclei.

4.2. *Stellar kinematics*

The measurements of the stellar velocity field with pPXF is shown in figure 8. In this routine we excluded the chip gap regions of the spectra in the fitting procedure, thus avoiding any interpolation errors as described

in section 2.5. In looking at the measured velocity field, there is an obvious rotation in the underlying stellar population, and the central sources show no signifiant difference in velocity - indicating that there is no kinematic decoupling of the off-center nucleus.

We compare the absorption line velocities of our two pure-absorption fitted spectra, and with the best fit template derived in the pPXF routine, as measured by `fxcor` and `xcsao` in figures 9 and 10, respectively. In both cases we see the same velocity field as measured by pPXF with `rv.fxcor` and `rvsao.xcsao` using the best-fit template. This is not the case, however, for the two pure-absorption fitted spectra. We find that both `fxcor` and `xcsao` and particularly sensitive to small residual features left over from an imperfect fit and subtraction of the emission lines and the interpolation artifact over the chip gap caused when mosaicking the 3 CCDs. As our spectral range is short, limiting it further by masking or avoiding these small features is not ideal.

In addition, a slight difference between the measured velocity field is observed for the `fxcor` and `xcsao` procedures given the exact same spectra - where this difference is minimized where the noise is small, such as with the pPXF best-fit template.
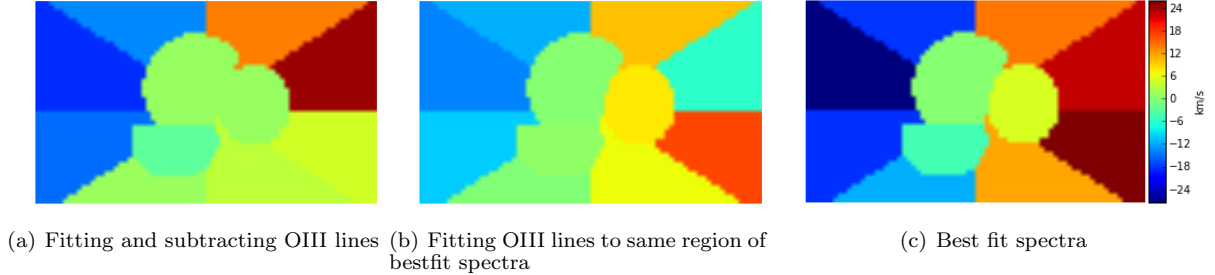
For these reasons we select pPXF as our preferred routine for it's ability to mask the emission lines effectively.
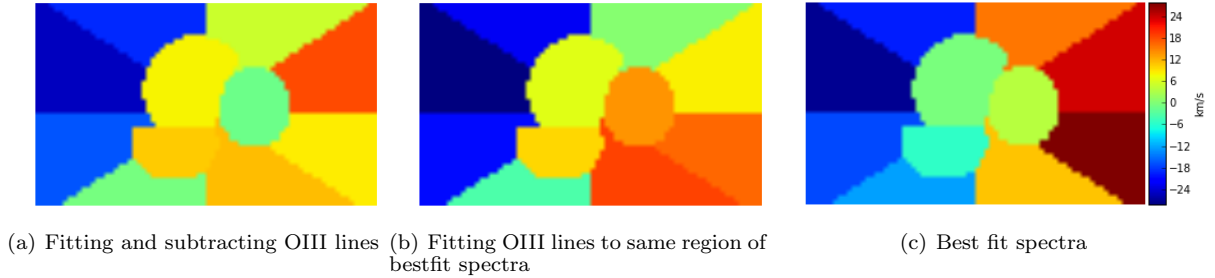
4.3. *Gas kinemtaics*

In measuring the gas kinematics, we use slightly modified velocity measurement techniques than for the stellar population velocities, and select a lower S/N of 20. The gas velocity field as measured by pPXF was obtained by fitting the galaxy spectra to a two-composite model of a pure gaussian-emission line spectra and a simple stellar population (SSP) template by the same optimiza-

(a) Interpolated velocity field   (b) Velocity measurement by bin
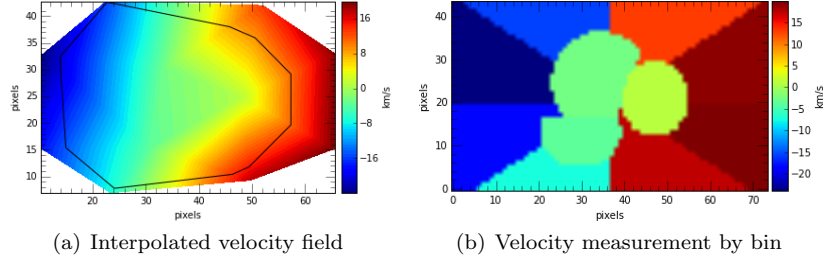
Figure 8. Stellar velocity field with pPXF at S/N ∼40, shown as a velocity field with 1 mag contours (a) and by the respective bins (b).

(a) Fitting and subtracting OIII lines   (b) Fitting OIII lines to same region of bestfit spectra   (c) Best fit spectra

Figure 9. Absorption velocity field with fxcor using various absorption spectra, S/N 40

(a) Fitting and subtracting OIII lines   (b) Fitting OIII lines to same region of bestfit spectra   (c) Best fit spectra

Figure 10. Absorption velocity field with rvsao using various absorption spectra, S/N 40

tion routine as described above. By this method both the stellar population velocities and the gas velocities may be measured. However, we find an unresolved issue with the absorption spectra fit by this method in that it does not agree with the results when only fitting the galaxy spectra to a single SSP - the measurements differ by $32\pm31\,{}^{km}/_s$. By visual inspection the fit with only the single SSP is closer to the galaxy spectra (omitting the emission lines) and this method is therefore used in the above analysis for the stellar population measurements.

The measurements of the emission velocities by this two-composite pPXF method agree closely with that measured from both `rv.fxcor` and `rvsao.emsao` with the exception of an unexplained feature over the central nucleus. In all cases the background gas is observed to exhibit rotation in the same direction of the stellar population, and there is no obvious decoupling of the off-center nucleus.
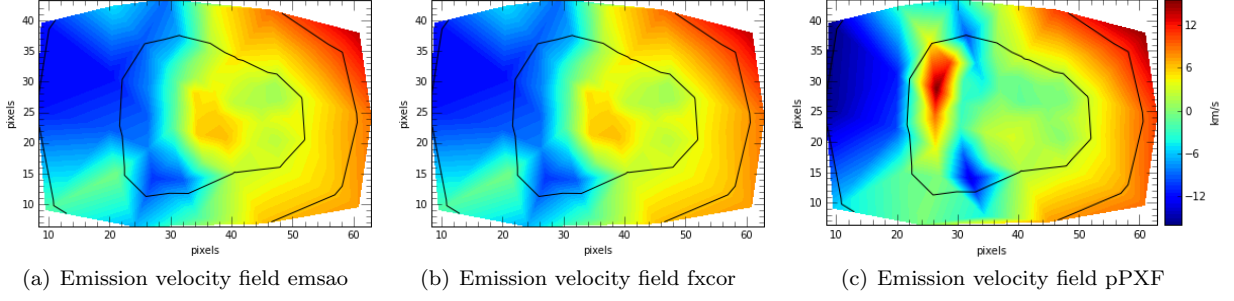
4.4. *Velocity field of stellar population and gas*

In order to determine if there is significant decoupling between the gas and stellar population we measure the gas velocity field as S/N 40 using the same method as described in the last section, and subtract field from that of the stellar population (see figure 12). We find the gas to be blue shifted, consistent with SDSS measurements of Gu et al. (2006), where the velocity difference between the stellar population and the gas is $\sim 20\pm 21\,{}^{km}/_s$. We observe no detectable KDC in the smooth rotating velocity field.

5. STELLAR POPULATION HISTORIES

To analyze the stellar population histories at the center of IC 225 we use Ulyss[7] (Koleva et al. 2009), a full-spectrum fitting technique which compares the galaxy absorption spectra pixel-to-pixel with an SSP built of non-linear components (age, [Fe/H], and [Mg/Fe]) convolved with a LOSVD and multiplied by a polynomial function. We investigated whether we could obtain the same measurements as Gu et al. (2006) of three populations of ages less than 100 Myr, between 100 and 1000 Myr, and greater than 1000 Myr with light fractions 40%,

---

[7] http://ulyss.univ-lyon1.fr/

(a) Emission velocity field emsao   (b) Emission velocity field fxcor   (c) Emission velocity field pPXF

Figure 11. Voronoi binned emission velocity fields at S/N 20, shown with 1 mag contours
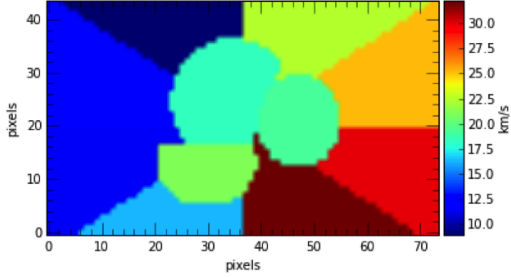
Figure 12. Velocity field of the stellar population with the gas velocities subtracted at S/N 40.

56% and 4% respectively. Gu et al. (2006) also predicts a metallicity of -0.65 from the metallicity-luminosity relation for elliptical galaxies. We also search for commonalities and/or differences between the binned sources

Although pPXF is also capable of providing mass fraction measurements, we choose to use Ulyss instead for it's easy implementation of multiple component SSP models with specific age and metallicity ranges.

We first assume a single SSP population for each region (central nucleus, off-center nucleus, tertiary flux source, and background) and explore the parameter space relations of age and metallicity with χ^2 maps for an age range of 20-14000 Myr. We use a different library of SSPs than for the kinematic analysis, Pegese.HR (Le Borgne et al. 2004) as it has a lower age limit than the MILES library. Although Ulyss has a function which removes emission lines in some of its tasks, there were unresolved errors in it's functionality with the χ^2 mapping task. We therefore choose to use the fitted pure-absorption spectra developed as described in the Appendix for our analysis of the SPHs (we do not use the best-fit pPXF template as Ulyss is not capable of resolving that a spectra is logarithmically binned). An example of fit of an absorption spectra is shown in figure 13.

A χ^2 map of the central nucleus (figure 14(a)) exhibits two local minima and one global minima of ages approximately 41 Myr with two different metallicities, and 800 Myr. Very similar minima are observed in the χ^2 map of the background (figure 14(b)). That the population ages at the minima are considerably young, we expect that a second older population exists but is perhaps obscured by the strong presence of the young stellar population.

We next assume two SSP populations: a young population of age range 20-800 Myr, and an old/intermediate age population of 800-14000 Myr. The χ^2 maps for the

two fitted SSPs of the central nucleus bin are shown in figure **??**. The results of the fit for each bin are shown in table 2.

| Bin	Age (Myr)	[Fe/H] (dex)	χ^2
Central nucleus	45	0.032	∼3.4
	2077	-0.97	∼3.4
Off-center nucleus	103	-0.30	∼6.6
	13604	-0.97	∼6.8
Dim flux source	30	0.032	∼3.8
	5392	-1.30	∼3.9
Background	103	0.032	∼4.8
	2076	-0.63	∼4.8

Table 2
Age and metallicities at the χ^2 minimum for young and old/intermediate aged populations. The χ^2 for each fit is shown as well, however we expect this value to not well represent the fit.

As expected, the metallicities of the younger populations are equal to or higher than older populations. We find that the intermediate aged population of the background bin has a metallicity which agrees with that predicted from the metallicity-luminosity relation of -0.65 dex (Gu et al. 2006). However, the central regions are observed to be much more metal rich, indicating localized enrichment at the center of the galaxy.

In assuming a three SSP population of age ¡ 800 Myr, 800 Myr ¡ age ¡ 5000 Myr, and 5000 Myr ¡ age ¡ 14000 Myr we find the light fraction to be approximately 60-80%, 20-40%, and 2-5% respectfully, which is roughly equivalent to the findings of Gu et al. (2006). The age restrictions applied by Gu et al. (2006) were not able to be reproduced due to limitations of the analyses technique of Ulyss. As old populations have been found in all studied dwarfs, the small light fraction of the old population does not necessarily indicate a lack of old stars, but a much stronger presence of a younger population.

We found the Ulyss program to give good, rough estimates of the stellar population histories, although it was difficult to obtain robust measurements. It was difficult to reproduce the results of the χ^2 minima by using the age and metallicity parameters of the reported minima as the initial parameters for a single fit to a galaxy absorption spectra. We also found the age and metallicity measurements for the single SSP fit task to be heavily dependant on the inital parameters - which was the motivation behind instead estimating the stellar population attributes from the χ^2 maps. These issues may
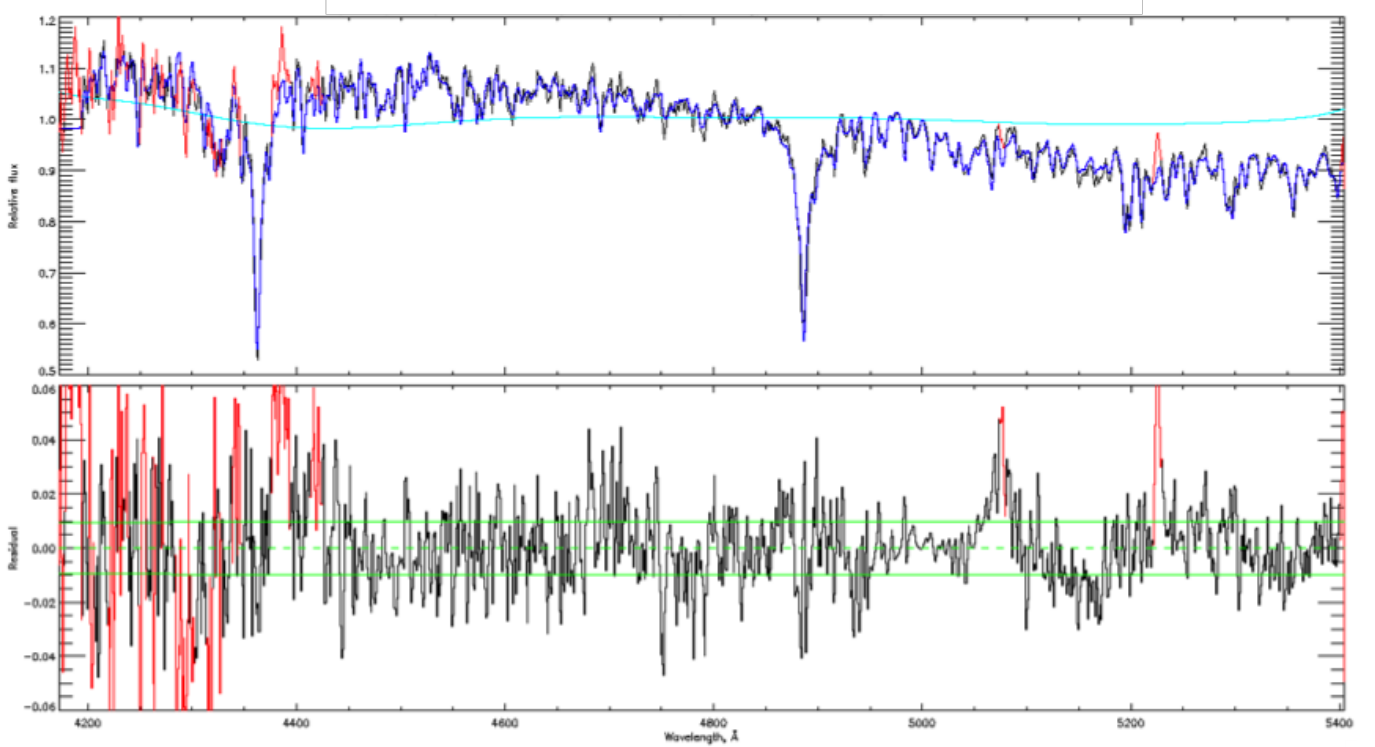
Figure 13. A single SSP fit to the galaxy spectra. The top panel shows the fitted pure-absorption spectra in black and the fitted SSP in blue, where large noise features have been removed from the fitting process, shown in red. The bottom panel shows the fit residuals, with green lines indicating a 1σ error.

(a) Central nucleus
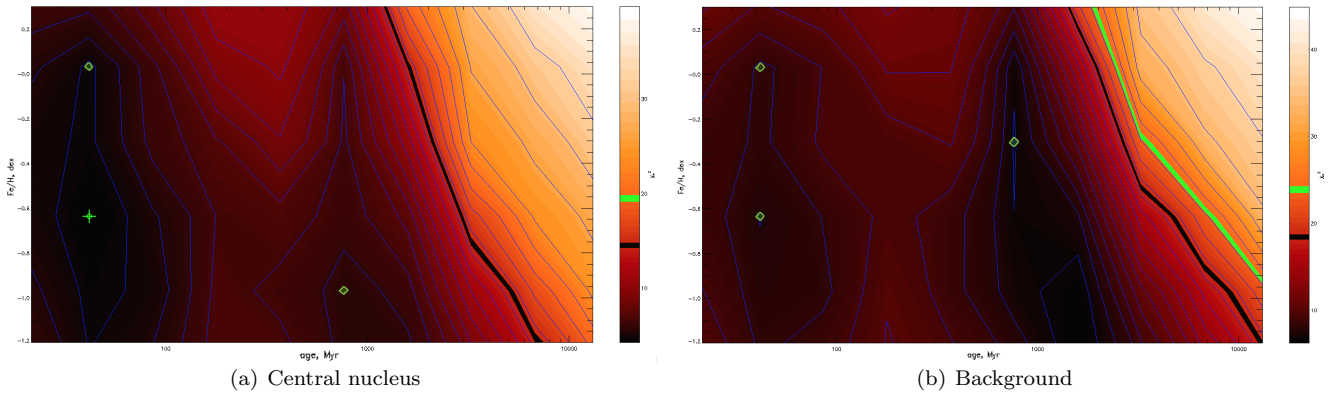
(b) Background

Figure 14. χ^2 maps with the fitted pure-absorption galaxy spectra fit to a single SSP. For both the central nucleus and the background three minima are observed - local minima labeled with green triangles, global minima with green crosses).

be resolved in an upcoming update of the Ulyss package (Philippe Prugniel, private communication).

6. CONCLUSIONS

In a comparison of several different reduction techniques with varying versions of the Gemini IRAF package, we determine the best procedure to use the modified package `ifudrgmos` for it's minimization of the wavelength shift discussed in section 2.2 and it's improved flat-fielding algorithm. Specifics of this reduction process are discussed in the Appendix.

With two-dimensional images of the continuum and emission regions of our galaxy spectra we observe the off-center nucleus to be significantly more luminous than

the central nucleus in the emission regions.

In the analyses of the kinematics of the stellar population and gas we compare three fitting techniques: pixel-by-pixel with pPXF, and cross-correlation with the `rv` and `rvsao` IRAF packages. In using the cross-correlation methods for measuring the stellar population kinematics we first needed to remove the emission lines from the galaxy spectra. This was achieved with two different fitting schemes. We found, however, that neither fitting routine was able to produce a pure-absorption spectra such that `rv.fxcor` nor `rvsao.xcsao` were able to reproduce the measurements of pPXF - where pPXF is able to distinguish the emission lines and remove them from the fitting process on its own. We attribute this to the small

(a) Young population   (b) Old/intermediate age population
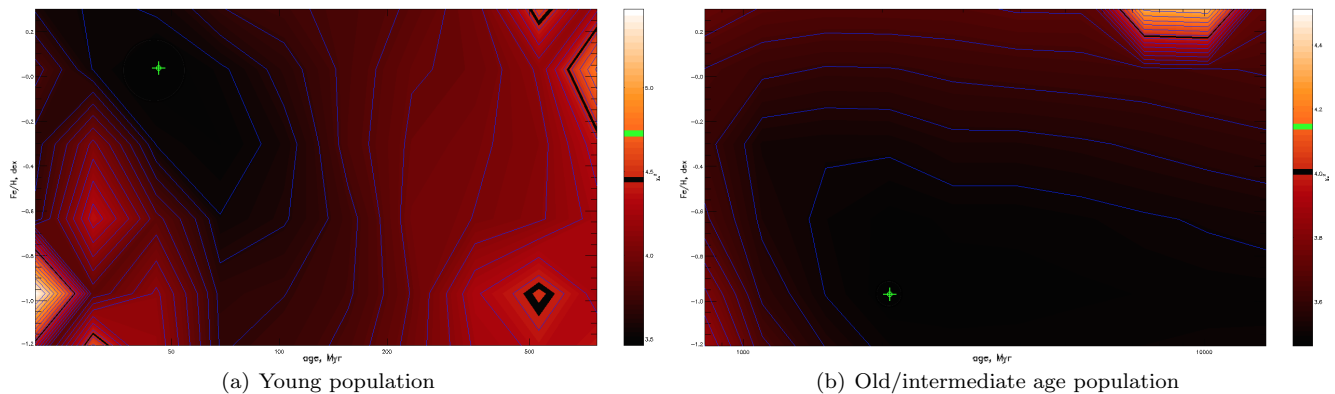
Figure 15. χ^2 maps with the fitted pure-absorption galaxy spectra of the central nucleus bin fit to a young and old/intermediate aged SSP. For both populations one global minima is observed, labeled as green crosses.

differences in the noise residuals left over from an imperfect fitting which affects the cross-correlation as well as a higher noise in general in the galaxy spectra than in the pPXF best-fit template. As the emission lines in our spectra are considerably stronger than the absorption features, this issue is not apparent when measuring the gas kinematics.

We detect rotation in both the gas and stellar population, where the gas is blue shifted by $\sim 25 \pm 21\,^{km/s}$ consistent with the prediction of Gu et al. (2006). We detect no obvious kinematic decoupling of any of the flux sources at the galaxy center, but rather a smooth velocity field.

The stellar population histories obtained from the χ^2 function in Ulyss were a good rough estimate of the stellar populations where we detected two SSP age populations with large light-fractions, and metal rich central region. The measurements of the metallicity of the underlying stellar population in the background of -0.65 dex agree with the predictions of the metallicity-luminosity function of galaxies as calculated by Gu et al. (2006).

From the above analysis we may constrain the formation and evolution process of IC 225. As the central region was found to metal rich we do not expect the secondary nucleus to be the result of a merging event with a dwarf galaxy or halo cluster. We also rule out the nucleus forming from a stripped or harassed spiral, as we observe the underlying stellar population to agree with the predicted metallicity of the metallicity-luminosity function for elliptical galaxies. Although IC 225 was found to have no detectable companion withing 30', we do not disclude a possible merging event with an enriched cluster as a possibility. To be able to distinguish further we require additional analysis of this dwarf elliptical.

7. FUTURE RECOMMENDATIONS

It may be possible to better assess the presence of a possible kinematic decoupling by first fitting a rotation model to the measured velocity fields, and subsequently subtracting the model to check for residuals. This would be more a rigorous analysis in that it would detect any small scale decoupling which is not obvious from observing the velocity fields alone. It would also detect if the

core as a whole is decoupled, rather than the central flu sources being decoupled from each other.

A more traditional method for analyzing stellar population histories employs the use of Lick indices for measuring specific line strengths indicative of particular star formation processes. This is often a more precise method, and would provide additional information such as the mass fractions and light fractions, yet is much more heavily involved. It would be interesting to compare the results of the two methods to better assess the uncertainties of the measurements obtained with Ulyss.

An additional task that could be preformed with our observations of IC 225 is the confirmation of the nebular extinction calculated by Gu et al. (2006) by verifying the same $H\gamma/H\beta$ Balmer decrements. This could easily be achieved by adapting the algorithm by which we remove the emission lines by fitting a Gaussian-Lorentz function to measure the line strengths. As our spectral range is too short to observe the other necessary emission lines, we are unable to repeat the calculation in it's entirety.

8. PUBLICALLY AVAILABLE ANALYSIS PIPELINE

We intend to make the final reduction procedure selected for this data set (as described above, and in greater detail in the Appendix) publicly available through the Gemini Data Reduction User Forum along with the supporting tasks for the wavelength shift correction.

The kinematic analysis was performed with a Python pipeline which implements the Voronoi binning, and executes pPXF, `rv.fxcor`, `rvsao.xcsao`, and `rvsao.emsao`. The pipeline is current available from

APPENDIX

REDUCTION PROCEDURE

Our final reduction procedure, which we found to have the best wavelength solution which minimizes the velocity difference between the two slits, was with a modified version of the Gemini GMOS IRAF package *ifudrgmos* as described in Davies et al. (2015) and available from the Gemini Data Reduction User Forum, and an updated version of the task `ifuproc` available by request from ....? Here we include a detailed description of te reduction procedure, while highlighting the differences of *ifudrgmos* from the publicly available version (see Davies et al. (2015) for further details).

Preprocessing

The first step of the reduction process is the bias subtraction and overscan trimming preformed with the task `gfreduce` to remove the instrumental signature from the images. This corrects for some pixel-to-pixel sensitivity, non-uniform illumination, and inconsistencies in the electronics. At this stage our data are formatted as multi-extension fits (MEF) files in which each extension represents the spectroscopic data of each CCD for a given lenslet, and each row contains the spectrum.

We then process the photometric(?) standards with their respective flats and arcs with our `ifuproc` task. This includes creating an unmosaiced bad-pixel mask from the Gemini supplied mask arrays, and applying with the `addbpm` task to each of the flats and sciences. This masks pixel values with the interpolated values from a low-order one-dimensional fit of the continuum with the `gemfix` task. The spectra are the extracted from the IFU image, and a quick wavelength solution is calculated with `gfextract` and `gswavelength` under the wrapper `gfreduce`. A background mask is then created to isolate the regions between the image rows between the blocks of fibres that are unilluminated and subtracted, with `fndblocks` and `gfbkgsub` respectively. Davies et al. (2015) reports an order of magnitude improvement in the nominally unilluminated zero-levels with this process. We then re-extract the flat fields with the the scattered light subtracted image.

The wavelength calibration is then calculated from the extracted spectrum of the CuAr arcs provided by Gemini. By inspection we find the identification of the lines to be satisfactory for the 30-40 brightest lines. We then use this wavelength function in the quantum efficiency correction for the flat field.

The most significant difference between the public Gemini GMOS IRAF package and the *ifudrgmos* package is the algorithm which is used to determine the correction of the fibre throughput with `gfresponse`. It is now capable of accounting for spectral distortions, but without the use of twilight flats. The fibre throughput correction is then applied to the extracted flat spectra. We then continue the reduction of the flux standard by applying the scattered light subtraction, identifying and correction for cosmic rays with the `L.A. Cosmic` (van Dokkum 2001) wrapper `grspec` and `gemfix` – with *fixpix* option which shows a slightly imported solution than the solution of `gscrspec` alone – and correcting for slight difference in the quantum efficiency between each of the three CCDs, then finally mosaicking the CCDs together, applying the final wavelength transformation, and sky subtraction.

The standards were then combined, and the flux calibration function was calculated using `gscalibrate` interactively to ensure a good fit to the continuum

We then processed the science images following the same procedure with `ifuproc`. We include an additional step to correct for the slight velocity difference between the two slits, as described in section 2.3. This was calculated by comparing a simple statistic on the wavelength transformed and cross correlated arc images, and comparing the two sides of the mosaiced image. We applied the correction with `gfshift`, and repeated the cross correlation to ensure that the shift was sufficient.

We then applied the wavelength calibration to each science exposure as calculated from the flux standards, and resampled to 3D data cubes with `gfcube`, and aligned and mosaiced the cubes with the *PyFu* package.

Variance and data quality

The variance and data quality panes were first estimated from the random noise of a Poisson distribution and read noise in the bias subtraction, and were propagated throughout the reduction process. This avoids several limitations and inaccuracies in the handling of noise in the current task algorithms. As the variance was propagated, the standard uncorrelated error calculation corresponding to the arithmetic operations preformed on the science data was applied. Similarly, the same interpolations procedures as were used on the science data was preformed on the variance, ignoring small scale smoothing effects. The data quality plans for the detector defects, chip gaps, cosmic rays were kept separate throughout the propagation to ensure that only the proper information was applied at the appropriate processing stage.

This method differs from what was used in Rudie (2006), and as result our measured S/N differs significantly. In the method used previously, by which the variance was calculated in the extraction of the spectra from the image by `apall`, the variance does not accurately reflect the total read noise and Poisson noise at this point in the reduction, but rather differs by approximately a factor of 5, which is then propagated through the analysis such that the reported noise differs by approximately a factor of 2.5 from or measurements.

EMISSION LINE FITTING AND SUBTRACTION

We consider two methods for the isolation of the absorption spectra by removing the emission features. In the spectral range observed the Hβ and Hγ emission lines coincide with absorption features, where the [OIII] doublet does not. In both methods we fit the absorption features first by parameterizing the same region with a pVoight function

(Gaussian convolved with a Lorentz) of the best fit template as derived in the pPXF routine, and including that fit with a Gaussian and a Lorentz function – the latter which helps to replicate the broadening of the line due to the kinematics – to fit the emission line. The methods differ in how the isolated emission lines are fit.

We expect that the emission region can be fit with a pure Gaussian function, a Lorentz to replicate broadening, and fitting the underlying continuum with a linear function. However, for the majority of our spectra the [OIII] line fell on the chip gap, causing interpolation artifacts to be produced during the mosaicking of the 3 CCDs. As such, this line was non-symmetric, and Gaussian-Lorentz function could not be fit to the line. We also anticipate that this fitting procedure would fail where the emission line is not well isolated from other features.

The second method we use to remove the [OIII] lines is by interpolating across the region using the pPXF best fit template. This method was found to work well in practice, but results in some residual noise features slightly larger than the average noise of the spectra as the best fit template is logarithmically binned whereas the galaxy spectra has finer, linear binning. It is important to preserve the linear binning in this case for the following stellar population history analysis.

REFERENCES

J. Allington-Smith, G. Murray, R. Content, et al. Integral Field Spectroscopy with the Gemini Multiobject Spectrograph. I. Design, Construction, and Testing. PASP, 114:892–912, August 2002.

R. Augarde, A. Chalabaev, G. Comte, et al. Spectrographic study of a large sample of KISO ultraviolet excess galaxies. I. The data. A&AS, 104:259–270, April 1994.

R. Bender and J.-L. Nieto. Internal kinematics of low-luminosity ellipsoidal galaxies. A&A, 239:97–112, November 1990.

M. Cappellari and Y. Copin. Adaptive spatial binning of integral-field spectroscopic data using Voronoi tessellations. MNRAS, 342:345–354, June 2003.

M. Cappellari and E. Emsellem. Parametric Recovery of Line-of-Sight Velocity Distributions from Absorption-Line Spectra of Galaxies via Penalized Likelihood. PASP, 116: 138–147, February 2004.

M. Cappellari, E. Emsellem, D. Krajnović, et al. The ATLAS^{3D} project - I. A volume-limited sample of 260 nearby early-type galaxies: science goals and selection criteria. MNRAS, 413: 813–836, May 2011.

R. L. Davies, M. Schirmer, and J. E. H. Turner. The 'Green Bean' Galaxy SDSS J224024.1-092748: unravelling the emission signature of a quasar ionization echo. MNRAS, 449:1731–1752, May 2015.

S. de Rijcke, D. Michielsen, H. Dejonghe, et al. Formation and evolution of dwarf elliptical galaxies. I. Structural and kinematical properties. A&A, 438:491–505, August 2005.

Q. Du, V. Faber, and M. Gunzburger. Centroidal Voronoi Tessellations: Applications and Algorithms. *SIAM Review*, 41: 637–676, January 1999.

E. Emsellem, M. Cappellari, R. F. Peletier, et al. The SAURON project - III. Integral-field absorption-line kinematics of 48 elliptical and lenticular galaxies. MNRAS, 352:721–743, August 2004.

H. C. Ferguson and B. Binggeli. Dwarf elliptical galaxies. A&A Rev., 6:67–122, November 1994.

M. Geha, P. Guhathakurta, and R. P. van der Marel. Internal Dynamics, Structure, and Formation of Dwarf Elliptical Galaxies. I. A Keck/Hubble Space Telescope Study of Six Virgo Cluster Dwarf Galaxies. AJ, 124:3073–3087, December 2002.

Q. Gu, Y. Zhao, L. Shi, et al. IC 225: A Dwarf Elliptical Galaxy with a Peculiar Blue Core. AJ, 131:806–813, February 2006.

A. Guérou, E. Emsellem, R. M. McDermid, et al. The Next Generation Virgo Cluster Survey. XII. Stellar Populations and Kinematics of Compact, Low-mass Early-type Galaxies from Gemini GMOS-IFU Spectroscopy. ApJ, 804:70, May 2015.

I. M. Hook, I. Jørgensen, J. R. Allington-Smith, et al. The Gemini-North Multi-Object Spectrograph: Performance in Imaging, Long-Slit, and Multi-Object Spectroscopic Modes. PASP, 116:425–440, May 2004.

M. Koleva, P. Prugniel, A. Bouchard, and Y. Wu. ULySS: a full spectrum fitting package. A&A, 501:1269–1279, July 2009.

D. Le Borgne, B. Rocca-Volmerange, P. Prugniel, et al. Evolutionary synthesis of galaxies at high spectral resolution with the code PEGASE-HR. Metallicity and age tracers. A&A, 425:881–897, October 2004.

J. M. Lotz, B. W. Miller, and H. C. Ferguson. The Colors of Dwarf Elliptical Galaxy Globular Cluster Systems, Nuclei, and Stellar Halos. ApJ, 613:262–278, September 2004.

R. C. Peterson and N. Caldwell. Stellar velocity dispersions of dwarf elliptical galaxies. AJ, 105:1411–1419, April 1993.

B. Rojas, B. Miller, J. Lotz, and M. Hilker. Ages, Metallicities and Kinematics in Fornax dEs. In *American Astronomical Society Meeting Abstracts*, volume 36 of *Bulletin of the American Astronomical Society*, page 1492, December 2004.

G. Rudie. A Kinematic Study of IC 225, Gemini Multi Object Spectrograph Integral Field Unit Data of a Dual-Nuclei Dwarf Elliptical Galaxy. 2006. URL http://www.ctio.noao.edu/noao/sites/default/files/EPO/2006gwen.pdf.

S. F. Sánchez, R. C. Kennicutt, A. Gil de Paz, et al. CALIFA, the Calar Alto Legacy Integral Field Area survey. I. Survey presentation. A&A, 538:A8, February 2012.

P. Sánchez-Blázquez, J. Gorgas, N. Cardiel, and J. J. González. Stellar populations of early-type galaxies in different environments. II. Ages and metallicities. A&A, 457:809–821, October 2006.

M. Sarzi, J. Falcón-Barroso, R. L. Davies, et al. The SAURON project - V. Integral-field emission-line kinematics of 48 elliptical and lenticular galaxies. MNRAS, 366:1151–1200, March 2006.

P. G. van Dokkum. Cosmic-Ray Rejection by Laplacian Edge Detection. PASP, 113:1420–1427, November 2001.

L. van Zee, E. D. Skillman, and M. P. Haynes. Rotationally Supported Virgo Cluster Dwarf Elliptical Galaxies: Stripped Dwarf Irregular Galaxies? AJ, 128:121–136, July 2004.

A. Vazdekis, P. Sánchez-Blázquez, J. Falcón-Barroso, et al. Evolutionary stellar population synthesis with MILES - I. The base models and a new line index system. MNRAS, 404: 1639–1671, June 2010.